Journal of Inclusion Phenomena and Macrocyclic Chemistry (2022) 102:851–860
https://doi.org/10.1007/s10847-022-01164-z

ORIGINAL ARTICLE

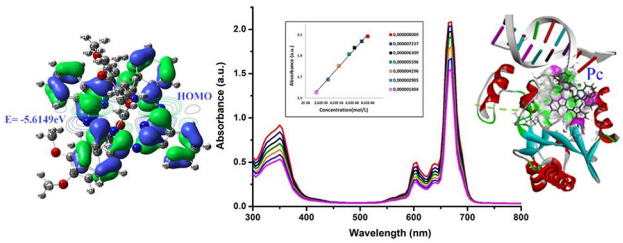
Synthesis of axially silicon phthalocyanine substituted with bis-(3,4-dimethoxyphenethoxy) groups, DFT and molecular docking studies

Derya Gungordu Solgun[1] · Aslihan Aycan Tanriverdi[2] · Umit Yildiko[3] · Mehmet Salih Ağirtaş[1]

Received: 27 July 2022 / Accepted: 12 September 2022 / Published online: 28 October 2022
© The Author(s), under exclusive licence to Springer Nature B.V. 2022

Abstract Axially bis-substituted silicon phthalocyanine was synthesized from the reaction of 2-(3,4-dimethoxy phenyl) ethanol and $SiPcCl_2$. The structure of the compound was justified by FT-IR, ^{1}H NMR, ^{13}C NMR, UV-Vis, and mass spectra. The conglomeration action of the phthalocyanine compound was determined by UV-visible spectra at different concentrations and in different solvents. Some parameters of this axial silicon phthalocyanine compound were investigated by computational chemistry. Structural optimization of axial silicon phthalocyanine substituted with compound, HOMO-LUMO energies and MEP maps was performed by density functional theory (DFT) studies. In addition, a chemical bond analysis of the molecule was performed with quantum theory atom in molecules (QTAIM). Finally, a molecular docking study was applied to this new phthalocyanine molecule in its binding mechanism.

Graphical Abstract Axially bis-substituted silicon phthalocyanine was synthesized by the newly designed reaction. The structure was characterized. Some parameters of this axial silicon phthalocyanine compound were investigated and analyzes were made with DFT studies and QTAIM. Finally, molecular docking work was applied.



Keywords Silicon phthalocyanine · Synthesis · Aggregation · Molecular docking · DFT · QTAIM

Introduction

Phthalocyanine compounds are in the group of macrocyclic compounds in terms of their chemical structures [1]. These compounds continue to be the subject of research for many researchers as a photosensitizing agent for gas sensors [2], electrochromic [3], pigments [4], solar cells [5], liquid crystals [6], nonlinear optics [7], catalyst [8], enzyme inhibition [9], antioxidant [10], antimicrobial [11], Antifungal [12], and photodynamic therapy [13]. It is known to be extensively researched for some types of cancer [14]. Especially, its use in new generation photodynamic therapy is promising for both patients and researchers. It has an important role in obtaining phthalocyanines synthetically. Because of this situation, significant changes in the properties of phthalocyanines can be created by binding groups with the desired

✉ Mehmet Salih Ağirtaş
salihagirtas@hotmail.com

[1] Department of Chemistry, Faculty of Science, Van Yuzuncu Yıl University, 65080 Van, Turkey

[2] Department of Chemistry, Faculty of Arts and Sciences, Kafkas University, Kars, Turkey

[3] Engineering and Architecture Faculty, Department of Bioengineering, Kafkas University, 36100 Kars, Turkey

solubility or intensity as substituents [15]. In this way, the compounds can be used for different purposes.

There is urgent research into the development of new treatment modalities for cancer. Photodynamic therapy is a candidate for the newest methods. Photodynamic therapy (PDT) involves cell damage [16] by reactive oxygen species (ROS) caused via the combined effect of light and molecular oxygen [17, 18]. In recent years, PDT is a clinically designed therapy for the care of certain types of cancer in which the patient can be treated continuously, regardless of dosage and symptoms. PDT is a suitable condition for increasing affinity toward cancers [19]. Phthalocyanine (Pc) has been recognized as one of the clinical photosensitizers with biocompatibility for antibiotics or anticancer drugs [18]. Recognizing how deformed nucleotides are positioned in the genome is vital to advancing cancer treatments. 8-oxo-7,8-dihydro-2′-deoxyguanosine (8-oxodGuo) and 4,6-diamino-5-formamidopyrimidine (Fapy• dG) [20] are formed by the opening of the imidazole ring followed by reduction. These enzymes hydrolyze the triphosphate form to remove the oxidized nucleotides in the nucleotide pondage and form the monophosphate form [20]. It is Aprataxin (APTX), which reverses DNA adenylation, although the context of deadenylation reparation is unclear. Reveals a mechanism for detecting and reversing adenylation in structure Aprataxin (APTX) reverses DNA adenylation -function applications of human APTX–RNA–DNA–AMP–metal complexes [21]. Several studies have examined whether the ribonucleotide regenerative limit is restored via Hnt3Aptx deficiency to determine whether APTX abolishes the vain ligation outputs produced at RNA-DNA junctions in vivo [21]. Various molecular dynamics simulation (MD) of phthalocyanines have been studied in the literature. Here, MD simulations of compound **3** [22] were performed. The interaction parameter electronegativity (χ) was computated to express the energy presenting the negative interactions occurring in metal complexes. Together with the calculated results, our simulation findings support the literature data [23].

QTAIM was used based upon the AIMAll program. Generally, a bond path (BP) and bond critical point (BCP), and chemical bonds between bonded atoms are demonstrated by theoretical studies [24, 25]. Each BCP gives the necessary chemical information that appropriately introduces the inside of the chemical bond. In BCP, electron density (ρ_{BCP}), laplacian electron density ($\nabla^2\rho_{BCP}$), electronic energy density (H_{BCP}), potential energy density (V_{BCP}), and kinetic energy density (G_{BCP}) are parameters and are used to characterize the defined chemical bond and non-chemical bond [26, 27].

In this study, bis-(3,4-dimethoxyphenethoxy) phthalocyaninato silicon (IV) was gained from the reaction of $SiPcCl_2$ and 2-(3,4-dimethoxy phenyl)ethanol. The compound was characterized by FT-IR, UV-Visible, Mass, ^{1} H-NMR, and ^{13} C-NMR spectroscopies. At the same time, density functional theory (DFT) studies were carried out. Chemical bond and non-chemical analysis of the molecule were done with QTAIM. The research was conducted on axial silicon phthalocyanine substituted with newly synthesized bis-(3,4-dimethoxyphenethoxy) groups for photodynamic therapy (PDT) cancer treatment.

Materials and methods

Materials

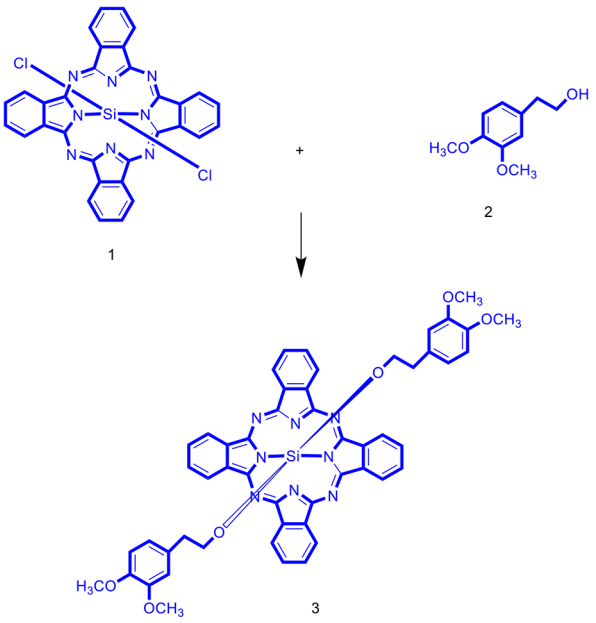
$SiPcCl_2$, 2-(3,4-dimethoxy phenyl)ethanol, K_2CO_3, toluene, THF, DMF, DMSO, $CHCl_3$, CH_2Cl_2, and ethyl acetate products used were obtained from Sigma-Aldrich, TCI, Acros, Alfa Aesar companies.

2.2. *Characterization*.

UV-visible spectra were projected onto the Hitachi U-2900 Spectrophotometer. Mass spectrum recordings were taken by LC-MS TOF electrospray ionization technique. Melting points were evaluated on an electrothermal (Stuart-SMP3) instrument. ^{1} H-NMR spectra were obtained in an Agilent with tetramethylsilane as standard. Recorded on a 400 MHz spectrometer FT-IR spectra were acquired on a Thermo Scientific FT-IR (ATR sampling accessory) spectrophotometer.

Simulations of the theoretical studies

All structural units were drawn in ChemDraw. The created molecules were converted to 3D MOL2 file type via Chem3D [23] In DFT studies on compound **3**, MOL2 files were transferred to Gaussian 09 W software, revision B.01 [28]. Compound **3** was optimized in the singlet state. Then, quantum chemical calculations of the optimized structures were carried out using the valence polarized basis set 6-311G together with the hybrid density functional Becke 3-parameter, Lee-Yang–Parr (B3LYP) [29]. Likewise, the becke with 3 parameters, Perdew-Wang 1991 (B3PW91) functional with the 6-311G basis set [30] was used to compare with this anecdote. In addition, the values of HOMO and LUMO energies and the values of HOMO/LUMO spaces were used to calculate the values of global reactivity parameters (GRP) [31]. A checkpoint file from Gaussian 09 W software was prepared using the B3LYP/6-311G functional. These files were converted to formatted checkpoint file type and transferred to the AIMQB system of the AIMAII program and the program was run [32]. Then, the parameters (values in the tables) of the AIM analysis in the literature



Scheme 1 Synthesis of bis −(3,4-dimethoxyphenethoxy)phthalocyaninato silicon (IV)

were calculated in the AIMStudio system connected to this program [33] and their images were taken [25]. The Maestro Molecular Modeling platform of the Schrödinger (version 11.8), LLC model was implemented via molecular insertion.[34–37] DNA polymerase beta substrate complex with templating cytosine and incoming Fapy-dGTP analog (DNA1) (PDB: 6DIA) [20], Human Aprataxin (APTX) bound to DNA, AMP, and Zn - product complex (DNA2) (PDB: 4NDH) [21] These DNA complexes, which are high resolution crystal structures, were Downloaded from http://www.rcsb.org/pdb.[37] 2D and 3D interactions were available by means of Discovery Studio (version 4.5) [38].

Synthesis of bis-(3,4-dimethoxyphenethoxy) phthalocyaninato silicon (IV) (3)

$SiPcCl_2$ (75 mg, 0.12 mmol), 2-(3,4-dimethoxyphenyl) ethanol (45.173 mg, 0.24 mmol) and K_2CO_3 (0.055 g, 0.39 mmol) dry toluene (10 mL) was stirred and refluxed for 30 h. After the product content reached 25 °C, it was separated with chloroform: water (organic fraction extraction process). After removing the THF solutes, the solvent was evaporated. The compound dissolves in THF, DMF, DMSO, $CHCl_3$, CH_2Cl_2 and ethyl acetate. Yield: 23 mg (21%), ^{1} H NMR (400 MHz, DMSO-d_6), (δ): 7.81 (s, 7 H), 6.82 (s, 7 H), 6.77 (s, 2 H), 6.70 (s, 6 H), 4.59 (s, 4 H), 3.70 (s, 4 H), 3.53, 3.36 (s, 6 H), 2.62 (s, 6 H), 2.48, 1.33. ^{13} C NMR (400 MHz, DMSO-d_6), (δ):169.69, 148.93, 147.49, 134.78, 133.03,132.37, 123.38, 121.08, 113.23, 112.26, 62.85, 55.97, 55.81, 40.12, 39.92, 39.71, 39.50, 30.85. IR (ATR), ν/cm^{-1}: 3057 (Ar-H), 2995,2933, 2835, 1726, 1591, 1514, 1463,1417, 1334, 1259,1232, 1138, 1026, 931,910,806, 759, 717. MS (ESI), (m/z): Calculated for $C_{52}H_{42}N_8O_6Si$: 902.3; Found: 903.30 [M + H]. UV–Vis (THF, 1×10^{-5} M): λmax/nm (log ε): 670 (5.32), 605 (4.73), 350 (4.99).

Results and discussion

Bis −(3,4-dimethoxyphenethoxy) phthalocyaninato silicon (IV) compound was gained from the reaction of 2-(3,4-dimethoxy phenyl)ethanol with $SiPcCl_2$ in a basic medium. Scheme 1 shows the synthesis route. The structure of the compound was characterized by UV-Visible, FT-IR, Mass, ^{1} H NMR, and ^{13} C NMR spectroscopies.

The compound shows its functional group with 3057 cm^{-1} vibrations (Ar-H) in the IR spectrum. The vibrations of 2995, 2933, and 2835 cm^{-1} correspond to the vibrations of the CH_3 group. 1591 and 1514 cm^{-1} vibrations show C = C vibrations. 1259 and 1232 cm^{-1} vibrations give C-O-C groups.

Aromatic protons are detected in the range of 7.81 to 6.70 ppm in the ^{1} H NMR spectrum of the compound. OCH_2 groups are seen at 4.59 ppm and CH_2 at 3.70 ppm. OCH_3 groups are observed at 3.36 ppm and 2.62 ppm. The peaks observed in the spectrum support the expected peaks in the structure. In the ^{13} C NMR spectrum, the carbons of the compound give the peaks of 169.69, 148.93, 147.49, 134.78, 133.03, 132.37, 123.38, 121.08, 113.23, 112.26 ppm. The peak of the OCH_3 group is observed at 62.85 ppm, OCH_2 at 55.89 ppm, and CH_2 at 30.88 ppm.

The absorbance values of the compound were measured as 670, 605, and 350 nm in THF solvent by UV-visible spectroscopy. These absorbance values correspond to the Q 670 nm and B 350 nm bands, which are characteristic of phthalocyanines. The value at 605 nm corresponds to the peak called the shoulder. The absorbance values of the compound at different concentrations are demonstrated in Fig. 1.

As seen in the figure, the compound exhibits non-aggregation behavior in the selected concentration range. The non-aggregation behavior of the compound is important as its potential to be used as a photosensor sensor. The electronic transitions of the compound in particular solvents are demonstrated in Fig. 2. The advantage that the compound is solvable in particular solvents is effective in using it easily in applications.

Molecular geometry

The optimized geometries of the molecule reveal that the specified metal elements protrude from its skeleton [39].

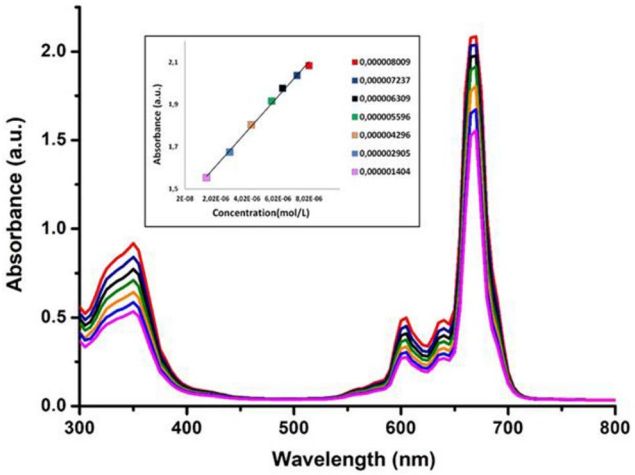


Fig. 1 In THF at different concentrations (1.40×10^{-6}- 8.01×10^{-6} M) UV-Vis spectra of compound **3**

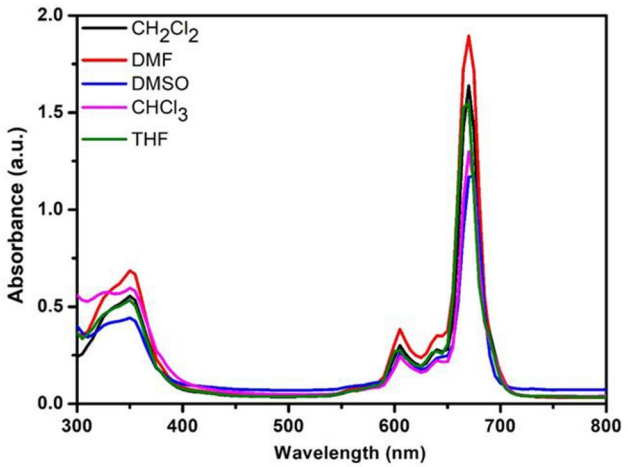


Fig. 2 UV-Vis spectra of compound **3** at CH_2Cl_2, DMF, DMSO, $CHCl_3$, and THF solvents

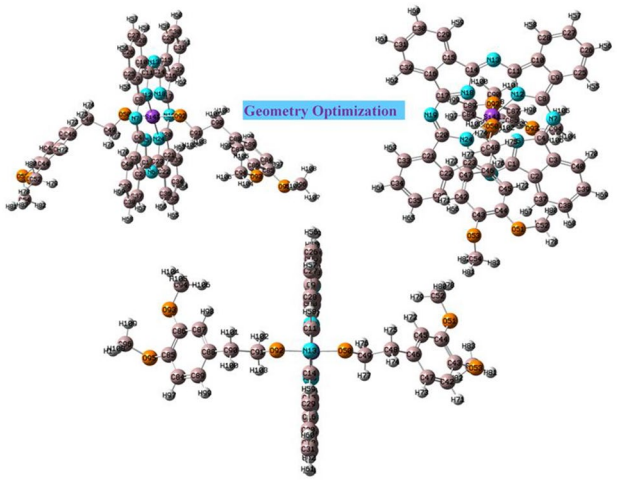


Fig. 3 Space image of composite **3** optimized (B3LPY/6-311G basis set)

The length of the C-C bond (d) is highly dependent on the type of transition metal. Also, the C-H bond lengths are not the similar. Although the values calculated by the two functionals are different, the trend in the C-O bond length in both calculations is interpreted into the effect of electron configuration and d-orbital splitting of the radii of the elements under investigation [39]. It was known that silicon phthalocyanine substituted with bis-(3,4-dimethoxyphenethoxy) groups has an axial structure. It can be predicted that the substitution of a carbon atom of compound **3** by a non-metal Si changes the symmetrical geometry. According to Fig. 3; Table 1, the average bond length and bond angles for each system were calculated using the B3LYP method 6-311G basis set and the B3PW91 method 6-311G basis set in the DFT system. In the results, the bond lengths of C-H, C-N, C = N, C-C, C = C, C-O, N-Si, Si-O are respectively calculated as 1.08 Å, 1.32–1.39 Å, 1.32–1.38 Å, 1.45–1.44 Å, 1.39–1.43 Å, 1.43 Å, 1.94–1.97 Å, 176 – 1.77 Å. Considering the triple bond angles, C-C-C 112°, C-C = C 106°, C-N-C 108°, C-C = N 123°, C-N = C 108°, N-C-N 127°, C-O-Si 131°, C-N-Si 125°, O-Si -O 173°, N-Si-N 179°, C-C-H 119°, O-C-H 111° and, C-C-O-C, C = C-C-H, O-Si-O-C, C = N-C = N, C-C = C-C dihedral angles were measured as 125 °, 179 °, 166 °, 179 °, 179 ° respectively.

Frontier molecular orbital analysis

HOMO and LUMO energies have a significant role in quantum chemistry, mostly in electrical and photonic properties [40]. The HOMO-LUMO separation in conjugated compounds is the result of vital intermolecular charge transfer from electron-donating groups to electron-accepting groups by the π-conjugate pathway. At the same time, the small energy gap that exists between orbitals draws attention to the transition state between orbitals, which leads to high reactivity [39]. In the DFT system using the B3LYP method 6-311G basis set and the B3PW91 method 6-311G basis set, the energies of molecular orbitals were computated to better understand the reactivity of the structural properties of a chemical compound. To a large extent, HOMO is localized around the core atoms of the available compound, while LUMO is located around the atoms. Table 2 lists the HOMO and LUMO energy ratings for the compound.

Figure 4 presents pictographic representations of orbitals for compound **3**. In the diagram, it is understood that the charge distribution takes place over the entire molecular system. The blue and yellow colored lobes indicate the positive charge, which are the HOMO orbitals, while the green and red colored lobes indicate the negative charge, which is the LUMO orbitals. Compound **3** showed nearly the same HOMO-LUMO energy gap of 2.1973 eV and 2.2178 eV, respectively. Here, it is predicted that the HOMO-LUMO

Table 1 Theoretically determined bond lengths (Å) and bond angles (°) of compound **3**

Bond lengths (Å)			Bond angles (°)		
Atom Groups	**B3LYP 6-311G**	**B3PW91 6-311G**	**Atom Groups**	**B3LYP 6-311G**	**B3PW91 6-311G**
C1-C2	1.451	1.447	C88-C90-C91	112.81	112.60
C4-N5	1.389	1.384	C9-C10 = C11	106.71	106.66
C14 = N13	1.325	1.322	C8-N12-C11	108.19	108.11
C16 = C32	1.394	1.391	C21-C20 = N19	123.53	123.38
C38-H68	1.081	1.082	C14-N18 = C17	108.07	107.98
C86-O93	1.397	1.390	N12-C11-N13	127.29	127.36
N24-Si41	1.971	1.962	C49-O50-Si41	131.05	130.31
N12-Si41	1.949	1.942	C20-N24-Si41	125.55	125.64
Si41-O92	1.771	1.766	O50-Si41-O92	173.25	173.36
Si41-O50	1.771	1.766	N12-Si41-N24	179.67	179.73
C49-O50	1.435	1.429	C26-C27-H57	119.25	119.23
C91-O92	1.435	1.428	C34-C35-H65	119.21	119.19
C23 = N6	1.326	1.323	O50-C49-H76	111.06	111.20
C20-N24	1.390	1.386	C42-C43-O53-C54	125.61	125.02
C17 = N18	1.387	1.383	C86 = C85-C84-H97	179.71	179.32
C28-H58	1.080	1.081	O50-Si41-O92-C91	166.39	163.72
C43-O53	1.398	1.392	C1 = N5-C4 = N7	179.84	179.79
C54-H83	1.086	1.087	C14-C15 = C29-C30	179.95	179.95

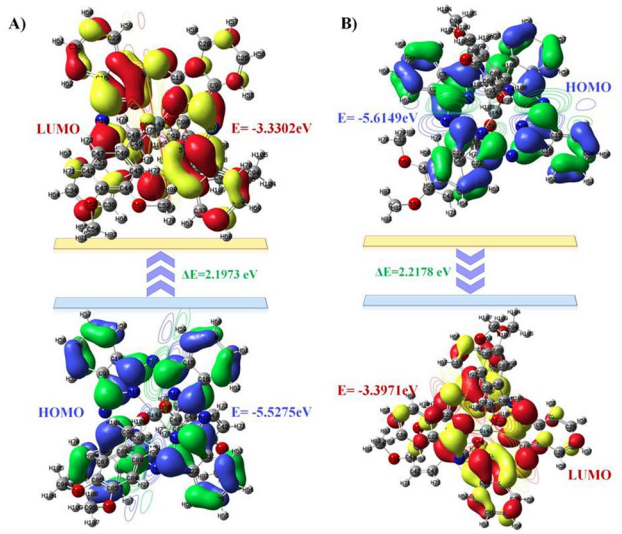


Fig. 4 A) B3LYP/6-311G, B) B3PW91/6-311G DFT_{HOMO} and DFT_{LUMO} of Atomic orbital composition of compound **3**

distribution on atoms may be responsible for the bioactivity of compounds with biological targets as intramolecular charge transfer occurs.

MEP analysis

The molecular electrostatic potential is generally defined as the measure of the strength of surrounding charges, nuclei, and electrons at a known location. The shape and size of the molecule, the colors, and the molecular electrostatic potential (MEP) are obtained [41]. The MEP diagram of the molecule is presented in Fig. 5. The positive and negative

Table 2 Comparison of energy gaps and properties of compound **3**

Molecules Energy	B3LYP	B3PW91
E_{LUMO}	-3.3302	-3.3971
E_{HOMO}	-5.5275	-5.6149
E_{LUMO+1}	-3.2774	-3.3419
E_{HOMO-1}	-5.7289	-5.7928
Energy Gap (Δ) $\lvert E_{HOMO}\text{-}E_{LUMO}\rvert$	2.1973	2.2178
Ionization Potential ($I = -E_{HOMO}$)	5.5275	5.6149
Electron Affinity ($A = -E_{LUMO}$)	3.3302	3.3971
Chemical hardness ($\eta = (I-A)/2$)	1,0986	1.1089
Chemical softness ($s = 1/2\eta$)	0.5493	0.5544
Chemical Potential ($\mu = -(I+A)/2$)	-4.4288	-4.506
Electronegativity ($\chi = (1+A)/2$)	2.1651	2.1985
Electrophilicity index ($\omega = \mu^2/2\eta$)	8.9269	9.1550

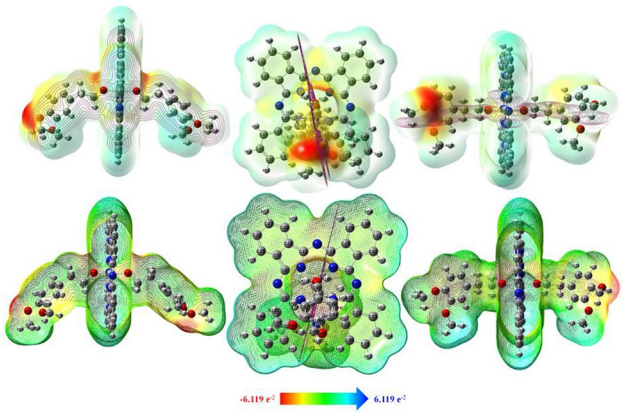


Fig. 5 Molecular electrostatic potential mapped of compound **3**

region of this compound represents between -6.119 e^{-2} and $+6.119$ e^{-2}. The most negative part is defined as the

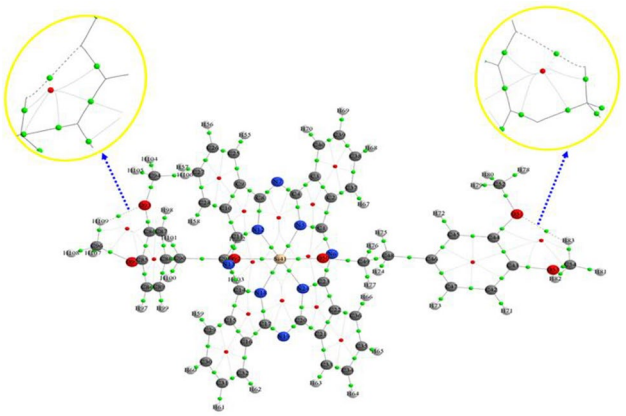


Fig. 6 Molecular Graph of Compound **3**

electrophilic region and is colored red. The most positive part is identified as the nucleophilic region and is indicated by the color blue. Here, it is thought that the reactive regions of compound **3**, which can be appropriately named depending on the proton and electron interactions, show biological activity.

QTAIM analysis

Study of H···O interactions

As is known, QTAIM analysis has become widespread as a suitable technique to study various molecular interaction patterns depending on electron density [42]. In QTAIM data, electron density not only characterizes the bond/interaction structure, but also classifies chemical bond/ interaction ways and distinguishes bond/ interaction strengths.[43, 44] If $\rho(r) > 0.1$, $\nabla^2\rho(r) < 0$ and $H(r) < 0$ (a.u.), it is known as a typical covalent bond. When $\rho(r) > 0$, $\nabla^2\rho(r) > 0$ and $H(r) > 0$, it is known as an ionic interaction. It is designated as an electron transfer bond if $0 < \rho(r) < 0.1$, $\nabla^2\rho(r) > 0$ and $H(r) < 0$ [45]. In light of the above discussion of QTAIM parameters, all bonds present topological properties of coherent electron density [46]. The V_{BCP}/G_{BCP} ratio of Bianchi et al. [47] indicates the intermediate ($1 < V_{BCP}/G_{BCP} < 2$) [48].

Thus, these bonds are low electron density values ($+0.01 < \rho(r) < +0.32$ a.u.) and large positive Laplacian values $\nabla^2\rho(r)$ from −0.88 a.u to +0.05 a.u. exhibits. Such parametric values describe ionic bonding, however negative H(r) values are seen in bond critical points (BCPs) (Table 3). Therefore, it states that there is a certain level of covalent in the molecule.

In addition, non-covalent interactions between molecular chains were also investigated. Various atom pairs are quite

Table 3 QTAIM parameters (all in a.u.) of compound **3**

Contact	ρ_{BCP}	$\nabla^2\rho_{BCP}$	G_{BCP}	V_{BCP}	H_{BCP}	δ
O51 - H83	+0.014626	+0.056649	+0.012289	-0.010415	-0.001874	+0.128048
O93 - H109	+0.014412	+0.055674	+0.012083	-0.010247	-0.001836	+0.131218
N13 - C14	+0.329257	-0.883184	+0.184774	-0.590344	+0.405570	+0.106522
C17 - N19	+0.328672	-0.879423	+0.185360	-0.590576	+0.405216	+0.105123
C20 - N24	+0.286566	-0.636879	+0.146112	-0.451445	+0.305332	+0.101149
C23 - N24	+0.284128	-0.624052	+0.143724	-0.443461	+0.299737	+0.102421
Si41 - O50	+0.095347	+0.468847	+0.142642	-0.168073	+0.025430	+0.039208
Si41 - O92	+0.095218	+0.468823	+0.142518	-0.167831	+0.025313	+0.039790
N24 - Si41	+0.072633	+0.217929	+0.079216	-0.103949	+0.024733	+0.130353
N5 - Si41	+0.072347	+0.217559	+0.078970	-0.103550	+0.024580	+0.130298
C54 - H83	+0.269628	-0.803932	+0.039801	-0.280585	+0.240784	+0.041753
C96 - H109	+0.269530	-0.803327	+0.039805	-0.280442	+0.240637	+0.041850
C90 - H101	+0.260528	-0.744211	+0.044948	-0.275950	+0.231001	+0.014115
C48 - H75	+0.260207	-0.742285	+0.044946	-0.275464	+0.230518	+0.014154
C9 - C10	+0.290333	-0.689986	+0.095053	-0.362604	+0.267550	+0.128265
C85 - O95	+0.253514	-0.451214	+0.181849	-0.476502	+0.294653	+0.038251
O95 - C96	+0.211846	-0.269662	+0.139534	-0.346483	+0.206949	+0.034651
O51 - C52	+0.218744	-0.290281	+0.151684	-0.375939	+0.224254	+0.010659
C42 - C43	+0.295565	-0.716029	+0.100812	-0.380630	+0.279819	+0.181184
C84 - C85	+0.295419	-0.715240	+0.100685	-0.380180	+0.279495	+0.180861
O93 - C94	+0.218743	-0.290440	+0.151586	-0.375783	+0.224196	+0.010524
O53 - C54	+0.211897	-0.269746	+0.139700	-0.346836	+0.207136	+0.034645

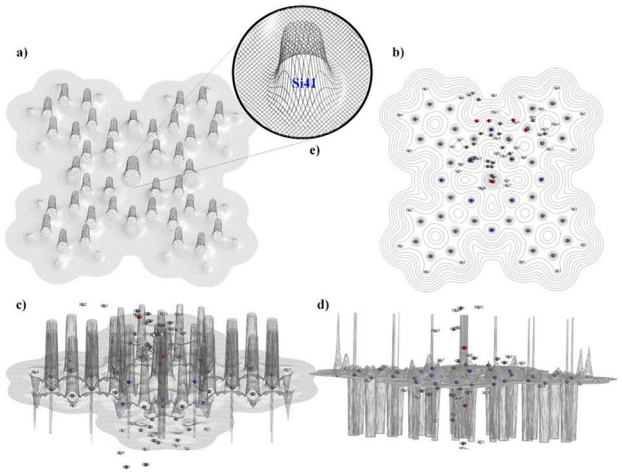


Fig. 7 Images of electronic charge density in the plane of compound **3**. (a) Relief map (Cores not shown.), (b) Contour drawings containing nuclei, (c) the relief map of the plane shown in (a) in the direction of electron density in which the nuclei are included, (d) the relief map of the plane shown in (a) in the direction of the Laplacian of the electron density into which the nuclei are included, (e) The plane perpendicular to the center of the Si core at its midpoint

common in QTAIM as it does not recognize H-bond interactions. The involvement of CH···OC interactions by QTAIM analysis was also investigated. The analysis parameters of the interactions are given in Fig. 6. Herein, H bonds were formed between O51-H83 and O93-H109, resulting from atomic convergence and the attraction force between O-H. These bonds are not chemical bonds. However, the formation of these bonds within the synthesized molecule itself is remarkable.

Charge density analysis

The charge distribution in the intramolecular system is the reflection of the physical forces in motion within the system [49]. Among them, the predominant force is the attractive force exerted with the help of nuclei, resulting from the positioned nature of the nuclear charge [50]. This interaction is liable for the single most significant topological feature exhibited by the molecular charge distribution of electron systems [51]. Recognizable atomic forms are created within the molecular charge distribution, as the charge density shows local maxima in nuclei [52]. These forms predominate in determining the nature of charge density, so their net features provide recognizable benefits to the features of the overall system [52]. Here, the local maxima in a load distribution are shown in Fig. 7. Charge density in compound **3** is represented in two ways, as a third-dimensional projection on the geometric plane and as a contour map where each contour represents a line of constant density. The charge distribution showed a maximum at the location of each core,

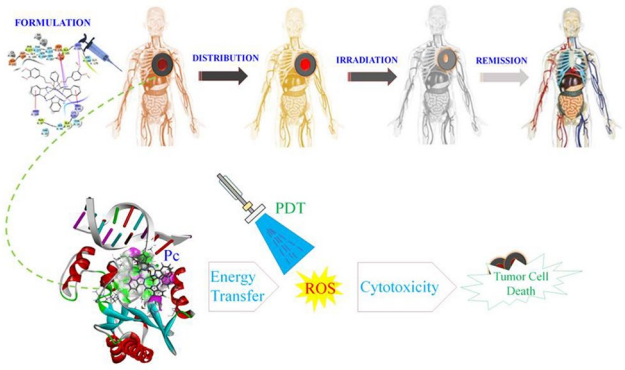


Fig. 8 Representative summary of PDT and ROS in Compound **3**

Table 4 Docking score of compound 3-DNA1 and compound 3-DNA2

Compound	Docking Score	
	DNA1 (PDB: 6DIA)	**DNA2** (PDB: 4NDH)
Compound **3**	-7.242	-5.202

which is the plane of the cores. Information of $p(r)$ in one or 2D was insufficient to characterize its 3D form. So what was needed was a method of concisely abridgment the fundamental topological features of a charge distribution.

Molecular docking studies

PDT is the newest form of treatment for some cancers. Pc is one of the clinical photosensitizers with biocompatibility for anticancer drugs [18]. Therefore, herein molecular docking studies were performed on DNA1 and DNA2 to interpret how damaged nucleotides are positioned in the genome. The Fig. 8, which is essentially a summary of PDT therapy, clearly states how compound **3** can be applied.

Molecular docking was performed to investigate the exact binding site and binding mechanism of ligand-protein interactions [53]. Compound **3** was prepared following previous practice with the Ligprep module. Protein preparation was put on hold for data using the wizard module. Then all the water molecules in the crystalline structure were expelled. Again with this module, the protein ion balance was optimized by determining the active site of the protein for flexible binding. Based on the receiver glide generation module, mesh boxes were created that license resilient docking by establishing networks at protein binding sites. The ligand-protein docking approach was carried out with the slip docking module. The lowest energy configurations show the highest binding affinity. Obtained docking scores are presented in Table 4, and interactions that occur as a result of molecular docking are presented in Table 5. Images of 2D and 3D interactions were obtained with the resulting

Table 5 Docking score of compound **3**-DNA1 and compound **3**-DNA2

	Code	Bond length (Å)	Type of bonding	Bonding point
DNA1	ASP A:192	2.80	Carbon Hydrogen Bond	Hydroxylated H
	SER A:187	2.84	Carbon Hydrogen Bond	Hydroxylated H
	ASP A:190	2.56	Carbon Hydrogen Bond	Hydroxylated H
	ARG A:183	2.40	Conventional Hydrogen Bond	Oxygen
	ASP A:276	1.66	Salt Bridge; Attractive Charge	H bound to amine
	ARG A:183	4.29	Pi-Cation	Benzene ring center
	ARG A:40,	3.50	Pi-Cation	Pyrrole ring center
	ALA A:43	5.34	Pi-Alkyl	Benzene ring center
	CA A:403	2.35	Metal-Acceptor	Hydroxylated H
DNA2	LYS B:274	2.49	Conventional Hydrogen Bond	Oxygen bonded to the benzene ring
	PRO B:271	2.82	Carbon Hydrogen Bond	Hydroxylated H
	LYS B:192	2.83	Pi-Cation	Benzene ring center
	LYS B:192	4.80	Unfavorable Positive-Positive	Bridge N
	LYS B:194	2.49	Carbon Hydrogen Bond	Bridge C
	LYS B:194	2.69	Pi-Cation; Pi-Donor Hydrogen Bond	Benzene ring center
	PRO B:196	4.60	Pi-Alkyl	Benzene ring center
	PRO B:196	4.95	Pi-Alkyl	Pyrrole ring center

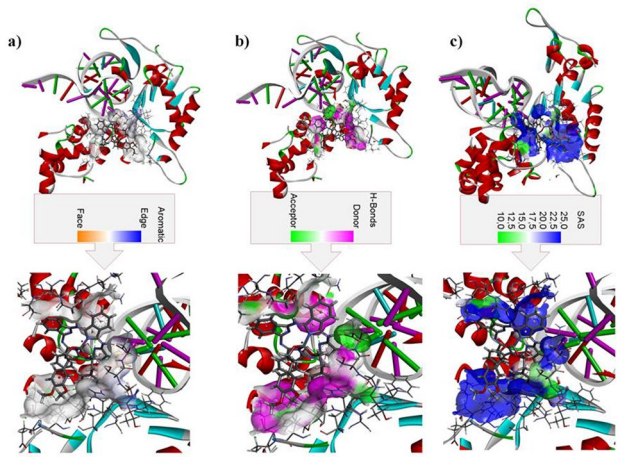


Fig. 9 3D view of (a) the aromatic surface on the receptor (b) hydrogen bond donor/acceptor surface on the receptor and (c) SAS surface on the receptor of compound 3-DNA1 interactions

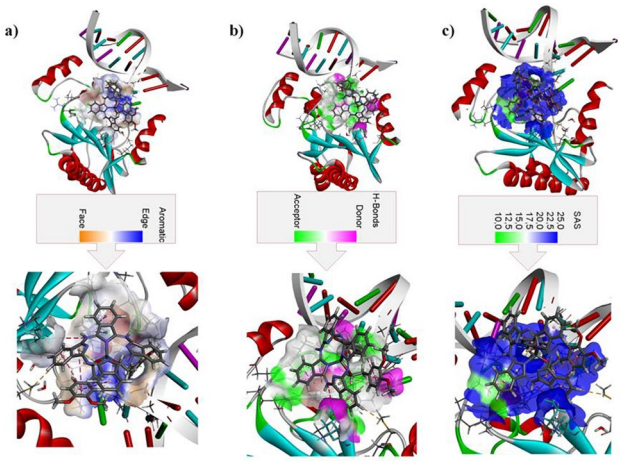


Fig. 10 3D view of (a) the aromatic surface on the receptor (b) hydrogen bond donor/acceptor surface on the receptor and (c) SAS surface on the receptor of compound 3-DNA2 interactions

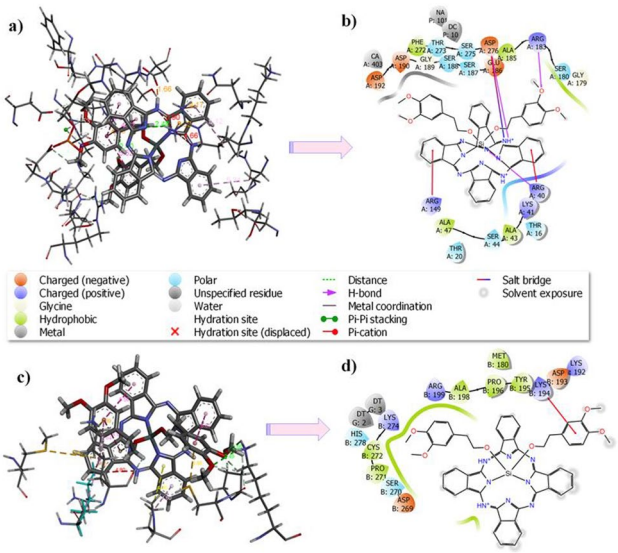


Fig. 11 2D view of **(a)** Compound **3**-DNA1 and **(b)** Compound **3**-DNA2 enzyme interactions

receptor model, Maestro 11.8 and Discovery Studio 4.5 (Figs. 9, 10 and 11).

As a result of the analysis, the receptor molecules examined by molecular docking analysis were determined and compound **3**-DNA1 was found to be more affective with the receptor glide score.

Conclusion

As a result, the original synthesis of the axial silicon phthalocyanine compound was made. The compound was characterized via FT-IR, UV-Visible, Mass, ^{1} H-NMR, and ^{13} C-NMR spectroscopies. Solubility and aggregation

properties of the compound were determined by UV-visible spectroscopy. N-Si bonds were found to have the highest values from the bond lengths calculated by the molecular geometry optimization of the DFT study. In addition, the N-Si-N angle measure is higher than the others in terms of triple bond angles. According to the HOMO-LUMO energy calculations, a higher eV value was obtained when the band gap was calculated with the B3LYP/6-311G basis set. Compound **3** has been shown to have biological activity by MEP analysis. Interestingly, CH···OC interactions were found in the molecule with QTAIM analysis and ∇2 ρBCP values of these bonds were positive. Charge density analysis was presented as a good method to briefly summarize the basic topological properties of the charge distribution of compound **3**. The receptor molecules examined in the molecular docking study were identified. It was determined that compound **3**-DNA1 compound was more effective with the receptor binding score.

Acknowledgements We would like to thank Van Yüzüncü Yıl University Scientific Research Projects Unit and Science Application and Research Center for their support (FBA-2022-9776).

Declarations

Conflict of interest The authors declare no conflict of interest.

References

1. Çakır, V., Arslan, T.: Synthesis and biological evaluation of new silicon(IV) phthalocyanines as carbonic anhydrase and cholinesterase inhibitors. Inorganica Chim. Acta. **530**, 120678 (2022)
2. Ağırtaş, M.S., et al.: Synthesis, characterization, and electrochemical and electrical properties of novel mono and ball-type metallophthalocyanines with four 9,9-bis(4-hydroxyphenyl)fluorene. Dalton Trans. **40**, 3315–3324 (2011)
3. Sridevi, B.R., Hoskeri, P.A., Joseph, C.M.: Effect of annealing on the optical, structural and electrochromic properties of vacuum evaporated manganese phthalocyanine thin films. Thin Solid Films. **723**, 138584 (2021)
4. Germinario, G., Werf, I.D., Sabbatini, L.: Pyrolysis gas chromatography mass spectrometry of two green phthalocyanine pigments and their identification in paint systems. JAAP. **115**, 175–183 (2015)
5. Ilgün, C., et al.: Novel Co and Zn-Phthalocyanine dyes with octa-carboxylic acid substituents for DSSCs. Sol. Energy. **218**, 169–179 (2021)
6. Zhou, J., et al.: Self-assembly and ionic conductivity of phthalocyanine-containing liquid-crystalline compound films. Thin Solid Films. **709**, 138148 (2020)
7. Ağırtaş, M.S.: Synthesis and characterization of novel symmetrical phthalocyanines substituted with four benzo [d] [1,3] dioxol-5-ylmethoxy groups. Inorganica Chim. Acta. **360**, 2499–2502 (2007)
8. Chen, L., et al.: Cobalt phthalocyanine as an efficient catalyst for hydrogen evolution reaction. Int. J. Hydrog Energy. **46**, 19338–19346 (2021)
9. Türkan, F., et al.: Determination of anticancer properties and inhibitory effects of some metabolic enzymes including acetylcholinesterase, butyrylcholinesterase, alpha-glycosidase of some compounds with molecular docking study. J. Biomol. Struct. Dyn. **39**, 3693–3702 (2021)
10. Ağırtaş, M.S.: Fluorescence properties in different solvents and synthesis of axially substituted silicon phthalocyanine bearing bis-4-tritylphenoxy units. Heterocycl. Comm. **26**, 130–136 (2020)
11. Sindelo, A., Mafukidze, D.M., Nyokong, T.: Fabrication of asymmetrical morpholine phthalocyanines conjugated chitosan-polyacrylonitrile nanofibers for improved photodynamic antimicrobial chemotherapy activity. Photodiagnosis Photody Ther. **38**, 102760 (2022)
12. Tang, F., et al.: Carboxymethyl chitosan-zinc(II) phthalocyanine conjugates: Synthesis, characterization and photodynamic antifungal therapy. Carbohydr. Polym. **235**, 115949 (2020)
13. Zhao, Y., et al.: A novel silicon(IV) phthalocyanine-oligopeptide conjugate as a highly efficient photosensitizer for photodynamic antimicrobial therapy. Dyes Pigm. **172**, 107834 (2020)
14. Zheng, B.-D., et al.: Recent advances in supramolecular activatable phthalocyanine-based photosensitizers for anti-cancer therapy. Coord. Chem. Rev. **447**, 214155 (2021)
15. Salih Ağırtaş, M.: Highly soluble phthalocyanines with hexadeca tert-butyl substituents. Dyes Pigm. **79**, 247–251 (2008)
16. Openda, Y.I., Babu, B., Nyokong, T.: Novel cationic-chalcone phthalocyanines for photodynamic therapy eradication of S. aureus and E. coli bacterial biofilms and MCF-7 breast cancer. Photodiagnosis Photody Ther. **38**, 102863 (2022)
17. Ezquerra Riega, S.D., et al.: Chalcogen bearing tetrasubstituted zinc (II) phthalocyanines for CT26 colon carcinoma cells photodynamic therapy. Dyes Pigm. **201**, 110110 (2022)
18. Lamch, Å., et al.: Folate-directed zinc (II) phthalocyanine loaded polymeric micelles engineered to generate reactive oxygen species for efficacious photodynamic therapy of cancer. Photodiagnosis Photody Ther. **25**, 480–491 (2019)
19. Matshitse, R., et al.: Photodynamic therapy characteristics of phthalocyanines in the presence of boron doped detonation nanodiamonds: Effect of symmetry and charge. Photodiagnosis Photody Ther. **37**, 102705 (2022)
20. Smith, M.R., et al.: A guardian residue hinders insertion of a Fapy•dGTP analog by modulating the open-closed DNA polymerase transition. Nucleic Acids Res. **47**, 3197–3207 (2019)
21. Tumbale, P., et al.: Aprataxin resolves adenylated RNA–DNA junctions to maintain genome integrity. Nature. **506**, 111–115 (2014)
22. Khnifira, M., et al.: A combined molecular dynamic simulation, DFT calculations, and experimental study of the eriochrome black T dye adsorption onto chitosan in aqueous solutions. Int. J. Biol. Macromol. **166**, 707–721 (2021)
23. Kaya, S., Kaya, C.: A new equation based on ionization energies and electron affinities of atoms for calculating of group electronegativity. Comput. Theor. Chem. **1052**, 42–46 (2015)
24. Grabowski, S.J., Ugalde, J.M.: Bond Paths Show Preferable Interactions: Ab Initio and QTAIM Studies on the X – H···π Hydrogen Bond. J. Phys. Chem. A. **114**, 7223–7229 (2010)
25. Huang, Q.-R., Kingham, J.R., Kaltsoyannis, N.: The strength of actinide–element bonds from the quantum theory of atoms-in-molecules. Dalton Trans. **44**, 2554–2566 (2015)
26. Abdolmaleki, A., Eskandari, K., Molavian, M.R.: Sulfonated or phosphonated membranes? DFT investigation of proton exchange in poly(oxadiazole) membranes. Polymer. **87**, 181–193 (2016)
27. Sangeetha, K., et al.: The study of inter and intramolecular hydrogen bonds of NLO crystal melaminium hydrogen malonate using DFT simulation, AIM analysis and Hirshfeld surface analysis. Mater. Today: Proc. **25**, 307–315 (2020)

28. Frisch, M.J., et al.: Gaussian 16 Rev. C.01. : Wallingford, CT. (2016)
29. Bourass, M., et al.: DFT and TD-DFT calculation of new thienopyrazine-based small molecules for organic solar cells. Chem. Cent. J. **10**, 67 (2016)
30. Chen, K., et al.: Unusual odd-electron fragments from even-electron protonated prodiginine precursors using positive-ion electrospray tandem mass spectrometry. J. Am. Soc. Mass. Spectrom. **19**, 1856–1866 (2008)
31. Mumit, M.A., et al.: DFT studies on vibrational and electronic spectra, HOMO–LUMO, MEP, HOMA, NBO and molecular docking analysis of benzyl-3-N-(2, 4, 5-trimethoxyphenylmethylene) hydrazinecarbodithioate. J. Mol. Struct. **1220**, 128715 (2020)
32. Pendás, Ã.M., Gatti, C.: 3 Quantum theory of atoms in molecules and the AIMAll software.J.C.B.A.43(2021)
33. Bensouilah, N., et al.: Host-guest complex of N-(2-chloroethyl), N-nitroso, N′, N′-dicyclohexylsulfamid with β-cyclodextrin: Fluorescence, QTAIM analysis and structure-chemical reactivity. J. Mol. Struct. **1146**, 179–190 (2017)
34. Yildiko, Ã., et al.: Synthesis, enzymes inhibitory properties and characterization of 2- (bis (4-aminophenyl) methyl) butan-1-ol compound: Quantum simulations, and in-silico molecular docking studies. J. Indian Chem. Soc. **98**, 100206 (2021)
35. TEKEŞ, A.T., et al.: Insilico Molecular Docking Studies of THBF Compound: TD-DFT Simulations and Drug Design. JIST. **11**, 2955–2966 (2021)
36. ; Schrödinger Release 2017-3: Schrödinger Suite 2017-3 Protein Preparation Wizard, Epik, Schrödinger, L.L.C., New York, N.Y., Impact, Schrödinger, L.L.C., New York, N.Y.: 2017; LigPrep, Schrödinger, LLC, New York, NY, 2017; Prime, Schrödinger, LLC, New York, NY, 2017; QikProp,Schrödinger, LLC, New York, NY, 2017. (2017)
37. Wang, G., et al.: Design, synthesis, biological evaluation and molecular docking studies of new chalcone derivatives containing diaryl ether moiety as potential anticancer agents and tubulin polymerization inhibitors. Bioorg. Chem. **95**, 103565 (2020)
38. BIOVIA Discovery Studio D. SYSTÈMES:. BIOVIA Corporate Europe, BIOVIA 334 Cambridge Science Park, Cambridge CB4 0WN, England. (2016). http://accelrys.com/products/collaborative-science/biovia-discovery-studio/
39. Rad, A.S., et al.: DFT calculations towards the geometry optimization, electronic structure, infrared spectroscopy and UV–vis analyses of Favipiravir adsorption on the first-row transition metals doped fullerenes; a new strategy for COVID-19 therapy. Spectrochim. Acta - A: Mol. Biomol. Spectrosc. **247**, 119082 (2021)
40. Karakas, A., et al.: Theoretical Diagnostics of Second and Third-order Hyperpolarizabilities of Several Acid Derivatives %. Open. Chem. J. **17**, 151–156 (2019)
41. Rahuman, M.H., et al.: Investigations on 2-(4-Cyanophenylamino) acetic acid by FT-IR,FT-Raman, NMR and UV-Vis spectroscopy, DFT (NBO, HOMO-LUMO, MEP and Fukui function) and molecular docking studies.Heliyon**6**, (2020)
42. Tosso, R.D., et al.: The electronic density obtained from a QTAIM analysis used as molecular descriptor. A study performed in a new series of DHFR inhibitors. J. Mol. Struct. **1134**, 464–474 (2017)
43. Fuster, F., Grabowski, S.J.: Intramolecular Hydrogen Bonds: the QTAIM and ELF Characteristics. T J. Phys. Chem. A. **115**, 10078–10086 (2011)
44. Yildiko, U., Tanriverdi, A.A.: A novel sulfonated aromatic polyimide synthesis and characterization: Energy calculations, QTAIM simulation study of the hydrated structure of one unit. BKCS. **43**, 822 (2022)
45. Jenkins, S., Morrison, I.: The chemical character of the intermolecular bonds of seven phases of ice as revealed by ab initio calculation of electron densities. Chem. Phys. Lett. **317**, 97–102 (2000)
46. Yildiko, U., Tanriverdi, A.A.: Synthesis and characterization of pyromellitic dianhydride based sulfonated polyimide: Survey of structure properties with DFT and QTAIM. J. Polym. Res. **29**, 1–17 (2022)
47. Bianchi, R., et al.: Multipole-refined charge density study of diopside at ambient conditions. Phys. Chem. Miner. **32**, 638–645 (2005)
48. Kamaal, S., et al.: A new copper(II)-based layered coordination polymer: Crystal structure, topology, QTAIM analysis, experimental and theoretical magnetic properties based on DFT combined with broken-symmetry formalism (BS-DFT). Polyhedron. **193**, 114881 (2021)
49. Zhao, D.-X., Yang, Z.-Z.: Theoretical Exploration of the Potential and Force Acting on One Electron within a Molecule. J. Phys. Chem. A. **118**, 9045–9057 (2014)
50. Zhou, H.-X., Pang, X.: Electrostatic Interactions in Protein Structure, Folding, Binding, and Condensation. Chem. Rev. **118**, 1691–1741 (2018)
51. Grishina, A.M., Potemkin, A.V.: Topological Analysis of Electron Density in Large Biomolecular Systems. Curr. Drug Discov Technol. **16**, 437–448 (2019)
52. Bader, R.F.W., Anderson, S.G., Duke, A.J.: Quantum topology of molecular charge distributions. 1. J. Am. Chem. Soc. **101**, 1389–1395 (1979)
53. ALTUN, K., et al.: Structural and spectral properties of 4-(4-(1-(4-Hydroxyphenyl)-1-phenylethyl) phenoxy) phthalonitrile: Analysis by TD-DFT method, ADME analysis and docking studies. IJCT. **5**, 147–155 (2021)

Publisher's Note Springer Nature remains neutral with regard to jurisdictional claims in published maps and institutional affiliations.

Springer Nature or its licensor holds exclusive rights to this article under a publishing agreement with the author(s) or other rightsholder(s); author self-archiving of the accepted manuscript version of this article is solely governed by the terms of such publishing agreement and applicable law.